International Journal of Fatigue 200 (2025) 109090

Contents lists available at ScienceDirect

International Journal of Fatigue

journal homepage: www.elsevier.com/locate/ijfatigue

Modeling the effect of TiN inclusion on fatigue lives of high-strength steel

Zikuan Xu [a], Peng Wang [a,b], Yichunxiang Shen [a,b], Peng Zhang [a,b,*], Bin Wang [a], Ziheng Shao [a,b], Zhefeng Zhang [a,b,*]

[a] Shenyang National Laboratory for Materials Science, Institute of Metal Research, Chinese Academy of Sciences, Shenyang 110016, China
[b] School of Materials Science and Engineering, University of Science and Technology of China, Shenyang 110016, China

ARTICLE INFO

Keywords:
Fatigue crack initiation
Fatigue life prediction
High-strength steel
Inclusion
TiN

ABSTRACT

In the present study, variability in high-cycle fatigue lives has been studied in AISI 52100 high-strength steel containing TiN inclusions at two heat treatment states. It is found that the spatial orientations of TiN inclusions in the samples are randomly distributed, and have no significant effect on their cracking behavior under cyclic stress. All the examined samples revealed that the fracture planes of TiN inclusion are approximately vertical to the loading axis. Accordingly, a fatigue life prediction model is proposed by taking into account the cracking behaviors of TiN inclusions, ultimately reducing the prediction error of fatigue lives to within 2.5 times of the experimental values. The model demonstrates that the size and shape of TiN inclusions significantly affect fatigue lives of the samples. Specifically, TiN inclusions in samples with longer fatigue life either has a small area perpendicular to the loading direction or is thin parallel to the loading direction. Overall, the comprehensive results regarding the effect of TiN inclusions on fatigue life highlight the strategies to minimize uncertainty in fatigue life predictions for high-strength steels.

1. Introduction

High-strength steel plays a pivotal role as a structural material due to its exceptional mechanical properties and its ability to withstand high loads [1]. Among the various attributes of high-strength steel, its fatigue properties are particularly crucial, as they govern the resistance of material to failure under repeated or cyclic loading conditions [2,3]. To ensure the safe and reliable service of structural components made of high-strength steel, the prediction and evaluation of its high-cycle fatigue (HCF) performance are of utmost necessity [4]. However, a notable challenge in the design of structures using high-strength steel is the inherent variability in its fatigue life, which necessitates the incorporation of significant safety margins to account for this uncertainty. Consequently, this leads to decreased energy efficiency and increased material consumption. Therefore, enhancing the prediction precision of HCF lives for high-strength steel has the great potential to optimize material usage and maximize the efficiency of structural designs.

In high-strength steels, the dispersion of fatigue lives is significantly influenced by the presence of inclusions, as demonstrated by numerous studies [5–8]. Due to cost constraints and typical steel manufacturing processes, the occurrence of inclusions is frequently unavoidable. Hence, quantifying the impact of these inclusions on fatigue life is of paramount importance. Various models have been developed to address this, including fatigue damage models [9–12] and predictive models for fatigue strength [13–15] and fatigue life [16–19]. However, given the characteristics of HCF, an error of 20 % in fatigue strength can lead to a life prediction error exceeding 500 %. Consequently, predicting fatigue life is considerably more challenging than predicting fatigue strength. Furthermore, the type of inclusions plays an important role in fatigue performance, and models that distinguish inclusion types often have higher accuracy in predicting fatigue life [6,7].

Consequently, researchers have conducted extensive studies on the impact of various inclusions on fatigue properties, such as Al_2O_3 [20,21], TiN [5,6,8,22,23] and MnS [7,24–26]. Among them, the hardness of MnS inclusions is relatively low, and they will deform during the rolling process, posing lesser threat to the fatigue performance of the materials, as evidenced by the statistical results of Spriestersbach et al. [27]. With regard to Al_2O_3 and TiN inclusions, Wang et al. [6,7] have shown that Al_2O_3 particles tend to be more rounded, whereas TiN particles exhibit a more angular shape. In terms of the stress concentration around inclusions, TiN is considered more detrimental to fatigue properties than Al_2O_3. Therefore, this study primarily focuses on the effect of

* Corresponding author at: Shenyang National Laboratory for Materials Science, Institute of Metal Research, Chinese Academy of Sciences, Shenyang 110016, China.
E-mail addresses: pengzhang@imr.ac.cn (P. Zhang), zhfzhang@imr.ac.cn (Z. Zhang).

https://doi.org/10.1016/j.ijfatigue.2025.109090
Received 21 February 2025; Received in revised form 20 April 2025; Accepted 30 May 2025
Available online 31 May 2025

TiN inclusions on fatigue lives in high-strength steel.

The cracking mechanism of samples containing TiN inclusions is generally accepted as follows: cracks initiate from TiN inclusions and then propagate into the matrix, leading to the final fracture [5,6,8,22,23]. In this context, the influence of TiN on the scatter in fatigue lives needs to be considered from two aspects: the cracking process within TiN itself (stage I) and the cracking process within the surrounding matrix (stage II). In stage I, factors such as the three-dimensional size, spatial orientation and fracture plane angle of TiN may all play different roles, yet few studies have considered this process [21,28]. In terms of statistical analysis, Wang et al. [21] introduced a stress relaxation coefficient to modify the stress intensity factor for cracked inclusions, aiming to improve the accuracy of life prediction. In terms of physical model that accounts for the inclusion cracking mechanism, currently, it is only found in the study by Chang et al. [28], but it remains a theoretical model without experimental validation. Therefore, it is imperative to conduct theoretical modeling and experimental verification of stage I. Additionally, the study about the spatial orientation of TiN in the fracture surface of sample under fatigue has not been reported to date, suggesting a need for the development of a characterization technique. Since TiN has a cubic unit cell with crystallographic orientations that resemble its external shape, electron backscattered diffraction (EBSD) technology can be used to characterize its orientation and thus determine its spatial orientation [29–31]. Furthermore, the issue of the fracture plane angle of TiN has also not been addressed to date. Prasad et al. [32] described a method employing tilt fractography technique to measure the fracture plane angle, which can be adapted to characterize the fracture plane of TiN inclusion.

In stage II, the primary factor influencing fatigue life is the size of TiN inclusions. Existing fatigue life prediction models, including the classical Murakami model [15,18], typically take into account the influence of inclusion size. The validity of the Murakami model has been demonstrated by numerous studies [33–37]. The essence of the Murakami model is that a small defect having cracks is equivalent to a crack having a shape identical to the projected shape of the small defect plus cracks. This aligns well with the cracking behavior observed in TiN in stage II, making it a particularly suitable tool for predicting fatigue life in materials containing TiN inclusions in stage II. However, a critical limitation persists: existing models, including the Murakami model, implicitly assume defects behave as pre-existing cracks without explicitly accounting for the nucleation processes intrinsic to TiN fracture. For TiN-specific cracking mechanisms, this oversimplification introduces predictive inaccuracies. Enhanced models must therefore integrate the unique fracture process of TiN to achieve more precise fatigue life predictions.

In this study, the effect of TiN inclusion on fatigue life, focusing on the three-dimensional size, spatial orientation and fracture plane angle of TiN, is revealed. The orientation of TiN inclusions is characterized using the EBSD. The fracture plane angle of TiN inclusion in HCF tested samples are characterized using tilt fractography technique. Besides, a fatigue life evaluation model considering cracking behavior of TiN inclusion is established. The objective of this study is to emphasize how to reduce the uncertainty in fatigue life prediction of the high-strength steels containing TiN inclusion.

2. Experimental methods

2.1. Material

AISI 52100 steel was employed in this study. The measured elemental compositions of the steel are listed in Table 1. The contents of all elements except for O and N were measured by inductively coupled plasma atomic emission spectrometer, and the contents of oxygen and nitrogen were analyzed by the oxygen–nitrogen-hydrogen analyzer. The rods with diameter of 13 mm and length of 105 mm were cut from the ingots by the wire electrical discharge machine. They were then austenitized at 850 °C for 30 min followed by oil quenching. They were tempered at 160 °C and 240 °C for 2 h and denoted as T160 and T240, respectively. To extract TiN inclusions and maintain their original 3D morphology, a non-aqueous electrolyte was employed, the details of which can be found in ref. [38].

2.2. Mechanical testing

The HCF tests were carried out on the GPS-100 fatigue testing machine at the stress ratio $R = 0.1$ (ratio between minimum stress to maximum stress), with a frequency of about 120 Hz based on the standard ASTM E466-21. The shape and size of fatigue sample is displayed in Fig. 1. The surface of fatigue sample was polished to achieve a mirror-smooth surface. The fatigue fracture morphology was observed using SEM (Quanta 600 and Zeiss SIGMA 500). The chemical composition of the inclusions at the fatigue crack origin was verified by the energy-dispersive X-ray spectroscopy (EDS) in SEM. The statistical analysis of fatigue data is based on the ISO 12107:2012(E) standard.

2.3. Characterization of fracture behaviors of TiN inclusions

The spatial orientations of the fracture planes of TiN inclusions, from which the cracks nucleate, have been determined using an SEM (Zeiss SIGMA 500). Following the works of Sinha et al. [39] and Prasad et al. [32], tilt fractography technique was employed in SEM by tilting the samples at different angles. Two fractured TiN inclusions with near-rectangle and incomplete rectangle shapes, respectively, are illustrated in Fig. 2a–d. Taking the near rectangle shape TiN inclusion as an example, four recognizable features on the fracture were identified, and one of these were chosen as origin and marked as 'O' in the image with other three non-collinear points marked as A, B and C as shown in Fig. 2a. All these points can also be recognized in Fig. 2c after tilting the sample by 70°. Following the method of Sinha et al. [39], the X, Y and Z coordinates of points A, B, and C in the SEM stage axes system were determined using (x, y) coordinates of the points A, B, and C, which were measured with respect to the origin 'O', at the tilt angles 0 and 70° (Fig. 2d and f). The calculation of Z coordinate is as follows:

$$Z = y_{70^\circ}/\cos(20^\circ) - y_{0^\circ}/\tan(20^\circ) \quad (1)$$

where y_{70° and y_{0° refer to the y coordinates measured at the tilt angles 0 and 70°. Then following the approach of Prasad et al. [32], the spatial orientations of the fracture planes of TiN inclusions can be obtained using the X, Y and Z coordinates of points A, B and C. Using the

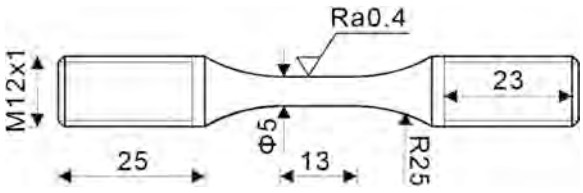

Fig. 1. Shape and size of experimental specimens with dimensions in mm.

Table 1
Measured elemental compositions (in weight percentage) of the AISI 52100 steels.

C	Cr	Mn	Si	Mo	P	S	Al	Ti	O	N	Fe
1.01	1.51	0.34	0.25	0.01	0.009	<0.003	0.010	0.006	0.0006	0.0078	Balance

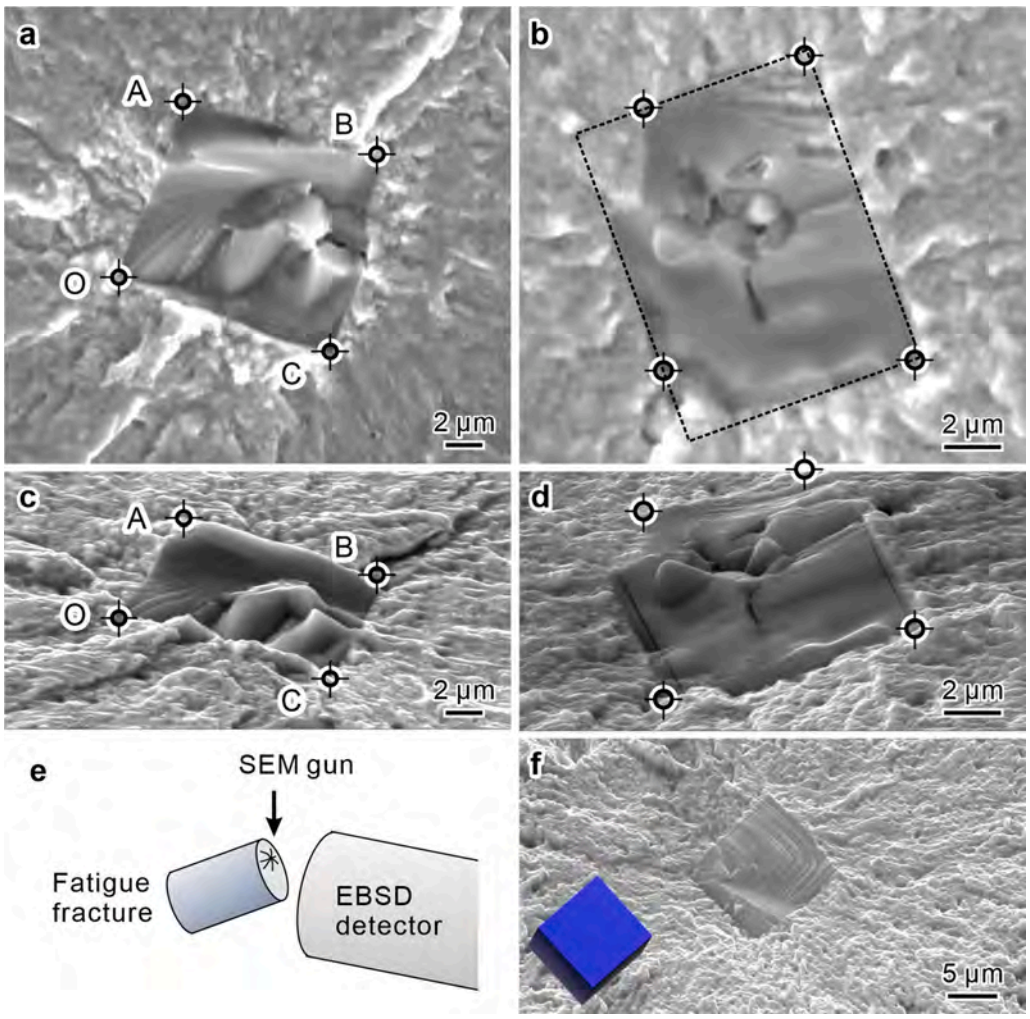

Fig. 2. Characterization of TiN orientation and fracture plane after failure: Fractography of TiN at tilt angle of 0° of (a) rectangle shape and (b) incomplete rectangle shape; fractography of TiN at tilt angle of 70° of (c) rectangle shape and (d) incomplete rectangle shape; (e) Schematic illustration of EBSD detector. (f) SEM image of TiN on the fatigue crack initiation site with crystal cell embedded on the lower left.

coordinates (X^A, Y^A, Z^A), (X^B, Y^B, Z^B) and (X^C, Y^C, Z^C), the cosine of angle between its normal vector and the loading axis could be calculated:

$$\cos(\theta) = \frac{(X^B - X^A) \times (X^C - X^B) + (Y^B - Y^A) \times (Y^C - Y^B) + (Z^B - Z^A) \times (Z^C - Z^B)}{\sqrt{(X^B - X^A)^2 + (Y^B - Y^A)^2 + (Z^B - Z^A)^2}\sqrt{(X^C - X^B)^2 + (Y^C - Y^B)^2 + (Z^C - Z^B)^2}} \quad (2)$$

2.4. Characterization of orientation of TiN inclusions

Typically, TiN inclusions exhibit a rectangular shape and their three perpendicular surfaces are aligned parallel to the (0 0 1), (0 1 0) and (1 0 0) crystallographic planes, respectively [29]. Consequently, the spatial orientations of the TiN inclusions can be represented by their crystallographic orientations, which were determined using an SEM (Zeiss SIGMA 500) equipped with EBSD detector (Oxford Symmetry S2), as schematically shown in Fig. 2e. TiN inclusions possess with rock salt type structure (space group $Fm\bar{3}m$) with a lattice parameter of a_{TiN} = 4.27 Å [40]. The EBSD patterns were acquired directly from the fracture of TiN inclusions without any polishing of the samples. A typical fractured TiN inclusion along with its spatial orientation were illustrated in Fig. 2f.

3. Results

3.1. Fatigue properties

The stress-life (SN) plots of the steels at T160 and T240 states are shown in Fig. 3a and b, respectively, and the applied load and number of loading cycles to failure are list in Tables 2 and 3, respectively. The Basquin law is employed to describe the relationship between the maximum stress and the fatigue life:

$$\sigma_{max} = \sigma_f (N_f)^b \quad (3)$$

where σ_f and b are material related constants. The data in Fig. 3a indicate that the steel exhibits variability in fatigue lives, where the maximum and minimum fatigue lives under the same stress amplitude

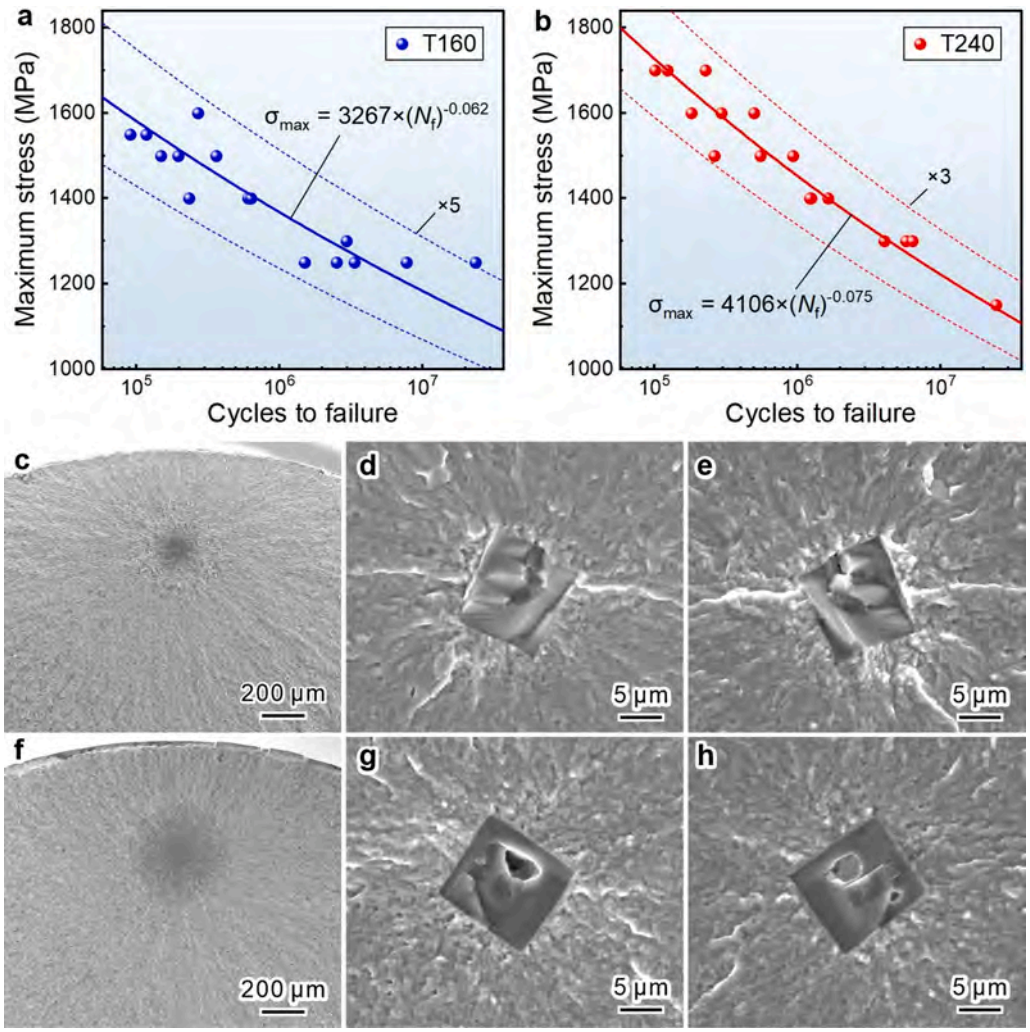

Fig. 3. S-N curve of the AISI 52100 steel at (a) T160 state and (b) T240 state. Typical fatigue fracture of AISI 52100 steel at (c-e) T160 state and (f-h) T240 state.

Table 2
Measurement results of TiN inclusions in the samples at T160 state.

Sample No.	Maximum stress (MPa)	Cycles to failure	N_1	N_2	*area** (μm^2)	*a* (μm)	*b* (μm)	*c* (μm)	Case	θ (°)
1#	1400	608,688	62,926	239,489	115	9.0	8.5	13.5	A	14.8
2#	1400	235,186	134,349	56,247	145	12.0	11.5	12.5	A	16.3
3#	1400	637,445	119,060	174,276	121	11.2	9.7	11.2	B	5.6
4#	1250	7,809,080	210,787	3,120,432	120	10.5	9.8	5.0	A	9.3
5#	1500	149,690	148,148	36,333	118	11.0	9.5	9.5	A	11.2
6#	1250	1,509,975	171,070	877,736	147	13.5	10.3	10.5	B	9.8
7#	1300	2,960,266	170,940	1,704,212	113	13.2	9.0	9.0	A	24.6
8#	1500	197,138	179,259	59,656	109	11.0	11.0	10.0	A	6.8
9#	1250	2,527,190	160,444	5,375,182	107	12.0	9.5	10.0	A	21.8
10#	1250	3,370,787	177,778	3,466,051	118	11.0	10.0	10.0	A	8.1
11#	1550	91,002	143,369	1031	183	13.9	12.0	12.0	B	27.4
12#	1500	363,214	148,148	282,292	85	8.0	8.0	8.0	A	18.1
13#	1250	23,627,498	113,778	16,421,906	92	10.6	8.0	10.0	A	10.0
14#	1600	270,641	138,889	34,291	92	10.2	9.0	9.0	A	25.0
15#	1550	117,890	70,251	168,083	81	8.5	7.0	10.0	A	5.4

* *Area*: the projected area of fractured TiN inclusion in the direction of the loading stress.

differ by up to about 20 times. In terms of the HCF behavior of high-strength steels [6,8,22], this level of variability is actually not considered significant. However, for engineering applications, there remains a desire for more accurate prediction of the fatigue lives in high-strength steels.

In order to analyze why the fatigue life of the present steels is dispersed, the fatigue fracture is characterized. After the fracture surfaces of all the HCF specimens were examined, the typical macroscopic fatigue fractures of samples at T160 and T240 states are shown in Fig. 3c and f, respectively. A typical radial pattern representing stable and unstable crack growth region can be observed on the fracture surfaces of all the samples at lower magnification images (Fig. 3c and f). In the fatigue cracking source, a TiN inclusion was observed to break in half and the fracture surfaces of TiN inclusions exhibit characteristics of

Table 3
Measurement results of TiN inclusions in the samples at T240 state.

Sample No.	Maximum stress (MPa)	Cycles to failure	N_1	N_2	*area*[*] (μm^2)	*a* (μm)	*b* (μm)	*c* (μm)	Case	θ (°)
1#	1300	5,779,499	1,569,859	721,598	60	7.5	7.5	3.5	A	4.4
2#	1400	1,252,656	203,175	2,865,816	91	10.2	8.0	10.0	A	17.2
3#	1500	264,351	222,551	367,255	114	13.2	6.5	7.5	B	28.3
4#	1500	554,652	283,952	682,564	98	10.3	9.3	9.5	A	17.5
5#	1600	296,523	123,457	193,235	103	10.0	8.0	12.0	A	6.4
6#	1600	499,132	277,778	269,150	95	9.2	9.0	9.0	A	4.8
7#	1600	182,695	277,778	27,328	166	13.0	11.0	11.0	B	13.7
8#	1500	938,168	249,504	1,165,826	86	9.5	7.8	8.5	A	3.6
9#	1150	24,635,867	477,128	16,190,495	131	13.0	10.0	9.0	A	0.7
10#	1400	1,227,033	286,508	1,533,461	106	11.5	9.5	10.0	A	14.6
11#	1300	4,066,909	308,547	2,238,835	130	10.5	9.5	10.0	A	13.9
12#	1700	124,120	261,438	16,191	148	11.0	8.8	8.8	B	8.3
13#	1700	101,645	211,765	27,548	130	11.0	10.8	12.0	A	25.1
14#	1700	228,932	261,438	63,586	106	8.0	6.5	6.5	A	19.7
15#	1400	1,646,656	353,714	436,876	144	12.0	9.5	9.0	A	5.0
16#	1300	6,401,889	271,598	3,571,337	116	9.2	8.2	9.2	A	11.3

[*] *Area*: the projected area of fractured TiN inclusion in the direction of the loading stress.

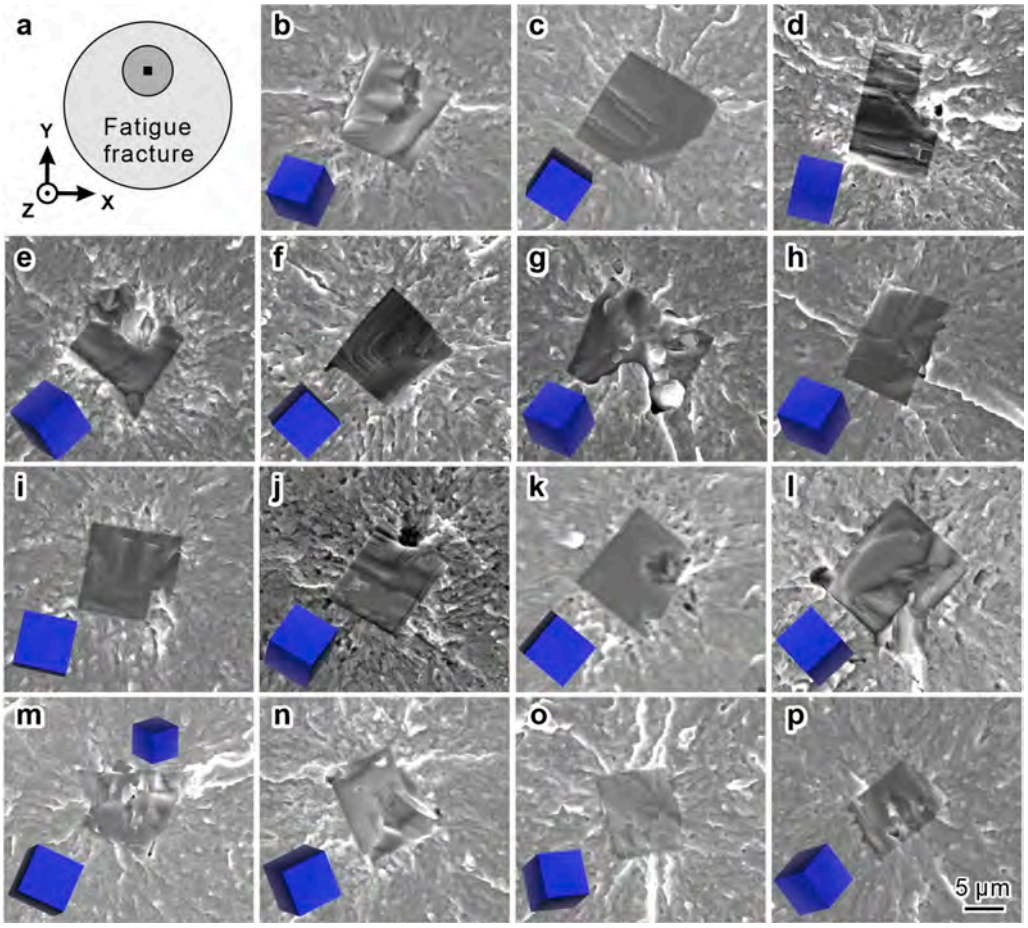

Fig. 4. SEM images of TiN on the fatigue crack initiation site of AISI 52100 steel at T160 state: (a) The schematization and (b-p) images of the fractures for specimens from 1# to 15#. The orientations of TiN inclusions obtained by the EBSD are embedded in the bottom left of each figure.

cleavage fracture (Fig. 3d, e, g and h).

3.2. Shape and dimensions of TiN

The SEM fractographies of the initiation site and characteristics of fatigue cracking around TiN inclusions in terms of its crystallographic shape and spatial orientation are shown in Figs. 4 and 5 for the samples at T160 and T240 states, respectively. Furthermore, the relationships between the fracture planes of the TiN inclusions and the spatial orientation of the crystallographic shape of the TiN inclusions are illustrated in Figs. 6 and 7. It can be seen that the shape and size of the fractured TiN inclusions are related to the spatial orientation and the dimensions of TiN crystallographic shape. There are two cases that exist. For case A, which is the majority, two dimensions of the TiN inclusions can be determined by theirs fractures (such as Fig. 6b). Because the fracture plane of TiN inclusions does not intersect with the upper or lower surfaces of the TiN inclusions, the height of the TiN inclusions cannot be determined. For case B, the fracture plane of TiN inclusions

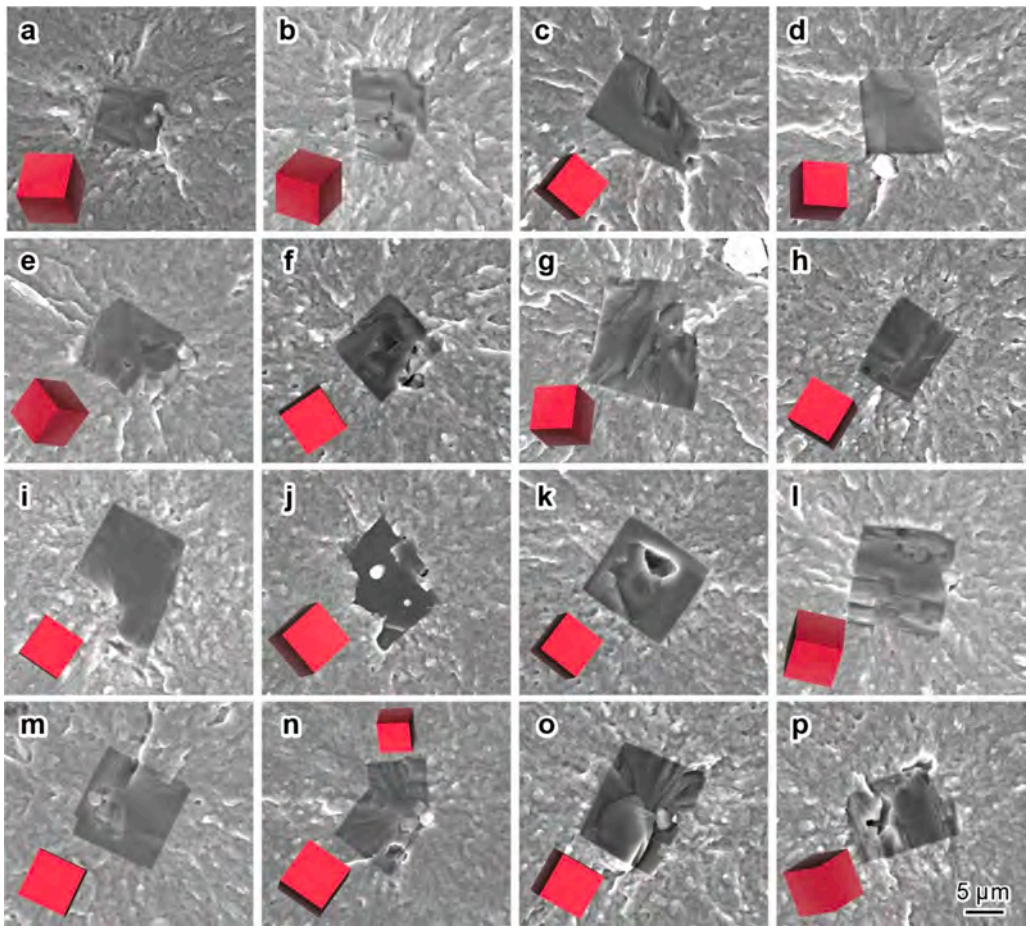

Fig. 5. SEM images of TiN on the fatigue crack initiation site of AISI 52100 steel at T240 state: (a-p) images of the fractures for specimens from 1# to 16#. The orientations of TiN inclusions obtained by the EBSD are embedded in the bottom left of each figure.

intersects with three of its orthogonal surfaces, so that all three dimensions of the TiN inclusions can be determined by its fracture morphologies, such as Fig. 6d. However, an assumption needs to be made that the area of the fracture plane should be as large as possible. This assumption is reasonable because larger fracture area of the TiN inclusions is generally more likely to cause the ultimate failure of sample [8]. Therefore, at least two (length and width) of the dimensions of each TiN inclusion causing the fatigue failure can be obtained by analyzing the results in Figs. 6 and 7, and the results are listed in Tables 2 and 3 for the samples in T160 and T240 states, respectively.

To gain a clearer understanding on the real shape of TiN inclusions in the present steel, the extraction experiments were conducted using non-fatigued materials, and the results of the extracted TiN inclusions are shown in Fig. 8a. Accordingly, the length and width of the TiN inclusion are defined as a and b with the longer side artificially designated as a (Fig. 8a). It can be seen that the actual shape of TiN inclusions is indeed rectangular, which proves the rationality of the above method. Accordingly, the ratio of a to b is calculated and the fitted normal distribution curve of a/b is displayed in Fig. 8b. The results show that 90 % of the a/b values are below 2. Based on the results above, the determination of c (height of TiN) for case A should ensure that the ratio of c to b is in the range of 0.5–2.

3.3. Cracking behaviors of TiN inclusions

The inverse pole figure of the spatial orientations of TiN inclusions in all samples is displayed in Fig. 9a. Approximately 50 % of TiN particles exhibit a preferential spatial alignment near the sample's Z-axis. Theoretically, TiN precipitate formation during solidification is a stochastic process [29–31], implying a uniform distribution of the spatial orientation of TiN inclusions throughout the material. However, fractographic analysis reveals a distinct non-random orientation of TiN particles. This anisotropic arrangement suggests that the spatial orientation of TiN significantly influences its cracking behavior. Furthermore, the characteristics of fracture planes of the TiN inclusions in terms of the angle between its normal vector and the loading axis, which is denoted as θ, are listed in Tables 2 and 3. All of the examined samples revealed that the fracture plane of TiN inclusions is nearly perpendicular to the loading axis. The fracture plane angle θ was found to be less than 20° in about 80 % of these samples. The maximum angle was found to be 28°, which corresponds to the sample (3# in T240) shown in Figs. 5c and 7c. The relative orientation of the fracture planes with respect to the sample axis, as depicted in Fig. 9b using inverse pole figures, provides further insight into the fracture behavior of the material under cyclic loading conditions.

The fracture characteristics of the TiN inclusions in terms of their crystallographic planes can be determined by combining the spatial orientations of the fracture planes with the crystal shapes. The inverse pole figure of the cracked crystallographic plane of the TiN inclusions in all samples is displayed in Fig. 9c. It can be seen that the cracked crystallographic planes are also randomly oriented. This is because the spatial orientation of TiN inclusions is randomly distributed and the TiN inclusions tend to cracking along the plane perpendicular to the loading direction.

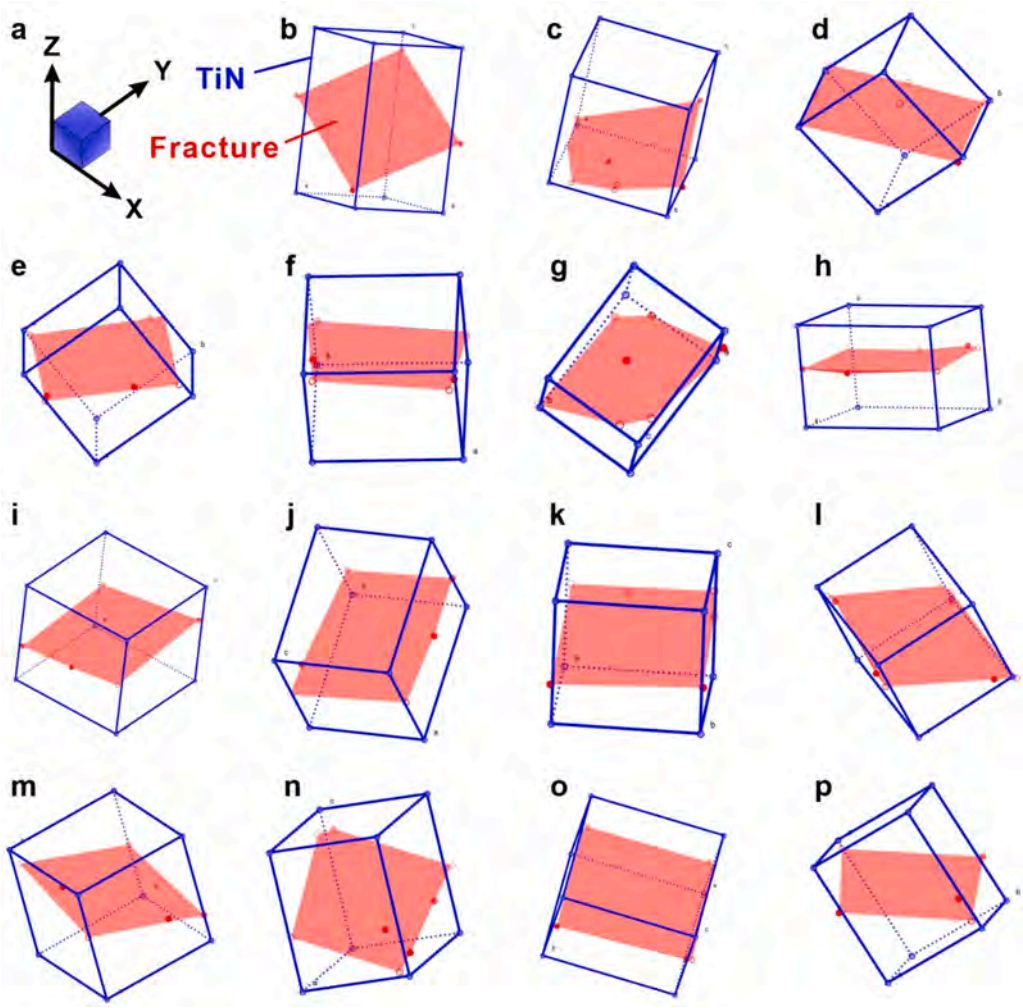

Fig. 6. Schematic illustrations of cleavage facet of TiN inclusion of AISI 52100 steel at T160 state: (a) Reference frame and (b-p) Fatigue samples from 1# to 15#.

4. Discussion

4.1. Fatigue cracking mechanism

In HCF, the entire fatigue life consists of short crack initiation and propagation processes [2]. In the present study, the open question is how to divide the overall process of TiN inclusion induced fatigue failure into initiation and propagation stages. This question can be approached by examining the fatigue failure mechanisms caused by inclusions, specifically, the direct crack initiation in the matrix around the inclusions [9,10,16,17,27], the inclusion-matrix interface debonding [21,41], and the inclusion cracking in the present study. Regarding the direct crack initiation near the inclusions, the distinction between crack initiation and propagation may not be highly sensitive, as the crack initiation life accounts for the majority in such cases [2]. For inclusions that undergo debonding or cracking during the fatigue process, the situation may become somewhat complex. The debonding at the interface leading to crack formation and the subsequent propagation of the crack may not constitute a continuous process and should be considered separately. This is also applicable for cracking of TiN inclusions in this study, where the cracking of TiN inclusions and the subsequent crack formation in the matrix may not form a continuous sequence. Consequently, for the fatigue failure caused by the TiN inclusions, we categorize the damage process into the first and second stages as schematically illustrated in Fig. 10. The most significant implication of this categorization is that the fatigue life of the first stage may no longer be significantly longer than that of the second stage.

4.2. Fatigue life prediction model

Chang et al. [28] have previously derived a two-stage model, in which dislocation accumulation leads to cracking of inclusions, ultimately resulting in fatigue fracture of the material. It is assumed that crack nucleation at a particle is the result of stress concentration at the particle–matrix interface described as piling-up of dislocations at the interface [28]. Chang et al. [28] identify two sequential steps: 1) fracture of the particle, and 2) propagation into the matrix, which is inherited in the present study. However, in the work of Chang et al. [28], the criterion for the crack of particle in stage I is when the bulk energy of the particle inclusions reaches a critical value. In this study, it is proposed that the bending stress on the surface of TiN inclusions, due to the piling-up of dislocations, should be used as a criterion for cracking when it reaches the required stress value σ_c. The bending stress σ_{bend} on TiN inclusions is calculated by:

$$\sigma_{bend} = \frac{\sigma_{dis} c^2}{3b^2} \geqslant \sigma_c, \tag{4}$$

where, σ_{dis} is the stress due to the piling-up of dislocations at the matrix-TiN interface. The definition of b and c can be seen in Fig. 10. The stress σ_{dis} is assumed to be proportional to the number of the piled-up dislocations, n [28]:

$$\sigma_{dis} = k_1 n, \tag{5}$$

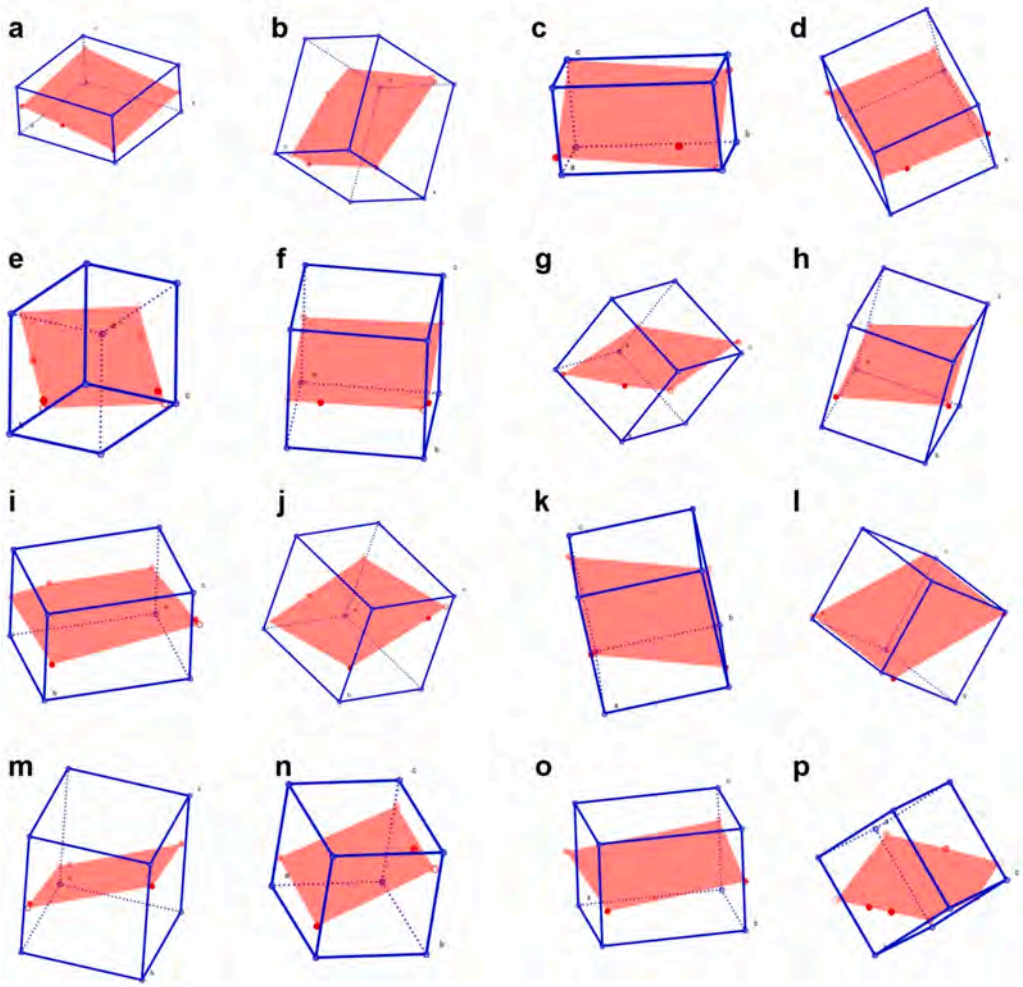

Fig. 7. Schematic illustrations of cleavage facet of TiN inclusion of GCr15 steel at T240 state: (a-p) Fatigue samples from 1# to 16#.

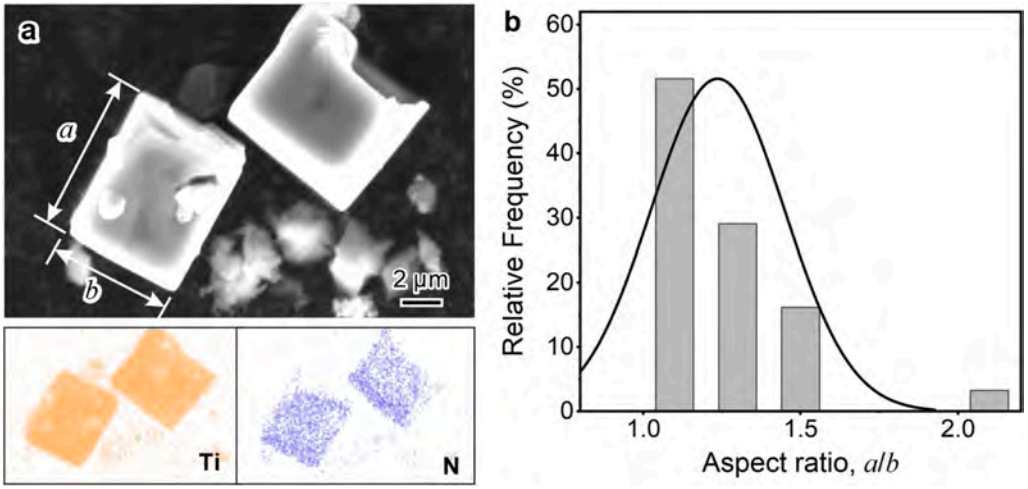

Fig. 8. (a) SEM microscopy of the extracted TiN inclusions maintaining their original 3D morphology and (b) Histograms and fitted normal distribution curve of aspect ratio a/b.

where k_1 is a material constant. Furthermore, it is assumed that for a given increment of fatigue cycles, dN, the increment of dislocations in the slip band is given by [28]:

$$\mathrm{d}n = k_2 D(\Delta\sigma - k_1 n)\mathrm{d}N, \tag{6}$$

where k_2 is a constant and D is the length of the slip band (see Fig. 10). Eq. (4) simply states that dn is proportional to dN and the slip band length D [42]. Integrating Eq. (4) yields:

$$n = \frac{\Delta\sigma}{k_1}\left(1 - \exp^{-Nk_1k_2D}\right). \tag{7}$$

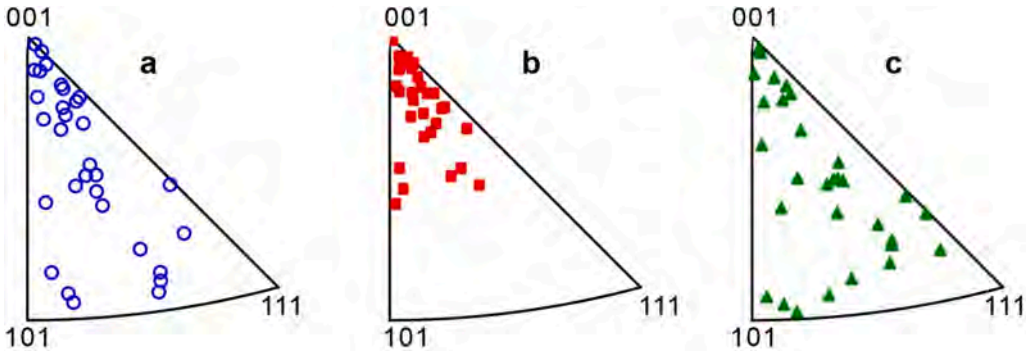

Fig. 9. Inverse pole figures of TiN and facet of GCr15 steels at T160 and T240 states: inclusions orientations along the Z axis; (b) Cleavage facets along the Z axis and (c) Cleavage facets along the [001] axis of the inclusion.

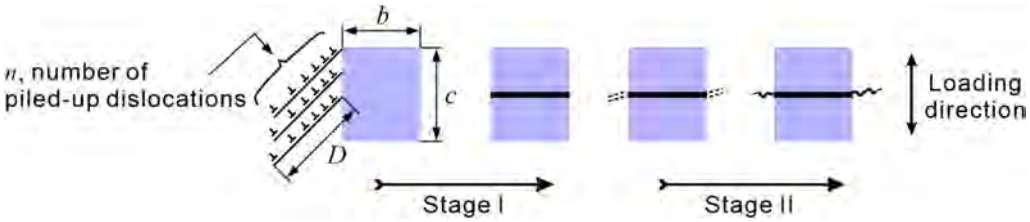

Fig. 10. A dislocation piling-up model for fatigue crack nucleation at TiN inclusion. Stage I: Fracture of the TiN inclusion due to stress concentration caused by piling-up of dislocations at the TiN-matrix interface. Stage II: Fatigue crack propagation into the matrix ultimately leading to failure of sample.

Substituting Eq. (7) into Eq. (5) and then the results in to Eq. (4) yields the critical condition for the stage I crack nucleation of the TiN inclusion:

$$\frac{\Delta\sigma c^2\left(1-\exp^{-Nk_1k_2D}\right)}{3b^2}\geqslant\sigma_c. \tag{8}$$

Taking the logarithm of Eq. (6) and rearranging, one finds the critical number of loading cycles as:

$$N_1=\frac{1}{-k_1k_2D}\ln\left(1-\frac{3b^2\sigma_c}{\Delta\sigma c^2}\right). \tag{9}$$

Expanding the logarithm term of Eq. (7) and keeping the first order term, one obtains:

$$N_1=\frac{3b^2\sigma_c}{k_1k_2D\Delta\sigma c^2}. \tag{10}$$

Merging all constants in Eq. (8), there is:

$$N_1=\frac{Ab^2}{\Delta\sigma c^2}\ \text{ with }\ A=\frac{3\sigma_c}{k_1k_2D}. \tag{11}$$

Eq. (9) is the expression giving the number of fatigue cycles N_1 required for the first stage for crack nucleation of the TiN inclusion.

The second stage of crack nucleation is the onset of crack advance from the cracked TiN inclusion into the ductile metallic matrix. The Murakami method is employed to model this stage [15]:

$$\Delta K_{\mathrm{TiN}}=Y\Delta\sigma\sqrt{\pi\sqrt{area}}, \tag{12}$$

where Y is the factor related to the location of TiN inclusion, $\Delta\sigma$ is the loading stress range and *area* is the projected area of fractured TiN inclusion in the direction of the loading stress. The correlation between ΔK_{TiN} and fatigue life is well established by [6,21,23]:

$$\Delta K_{\mathrm{TiN}}=\Delta K_{\mathrm{f}}(N_2)^m, \tag{13}$$

where ΔK_{f} and m are material related constants. Thus, the cycles, N_2, at which cracking extends into the matrix is:

$$N_2=\left(\frac{\Delta K_{\mathrm{TiN}}}{\Delta K_{\mathrm{f}}}\right)^{1/m}. \tag{14}$$

Therefore, the total fatigue life can be predicted by:

$$N_{\mathrm{f}}=\frac{Ab^2}{\Delta\sigma c^2}+\left(\frac{\Delta K_{\mathrm{TiN}}}{\Delta K_{\mathrm{f}}}\right)^{1/m}. \tag{15}$$

As can be seen from the deduction above, the characteristics of TiN inclusions now include *b*, *c*, and *area*, which are listed in Tables 2 and 3 for all the samples. Among the parameters, the value of *c* was determined under the constraints of the aspect ratio of TiN inclusion obtained from the non-fatigued material. The value of *c* is not unique; rather, it was selected among those that conformed to the aspect ratio distribution pattern, with the specific choice being the one that minimized the prediction error for fatigue life. Those material-related parameter values (A, ΔK_{f} and m) in the present model were obtained through fitting processes aimed at minimizing the overall error.

The fitting results only by the Murakami method and by the present model for samples at T160 and T240 states are shown in Fig. 11, and the predicted fatigue life of two stages are listed in Tables 2 and 3, respectively. It can be observed that when only the Murakami method is employed, the predicted fatigue lives are within 5 times of the experimental fatigue lives. For the present model, the predicted fatigue lives are within 2.5 times of the experimental fatigue lives.

It is worth noting that the parameters (ΔK_{f} and m) for Eqs. (10) and (11) are different because the fatigue life in stage I is considered. Furthermore, although the method used to determine the value of *c* for case A may limit the model's novelty and practical applicability, it reveals an insightful possibility based on the results: namely, that the fatigue life of TiN cracking can be more precisely characterized by segmenting it into two distinct stages, N_1 and N_2, thereby resulting in reduced prediction errors.

4.3. Effects of TiN inclusions on fatigue life

To better illustrate the effects of the size and shape of TiN inclusions

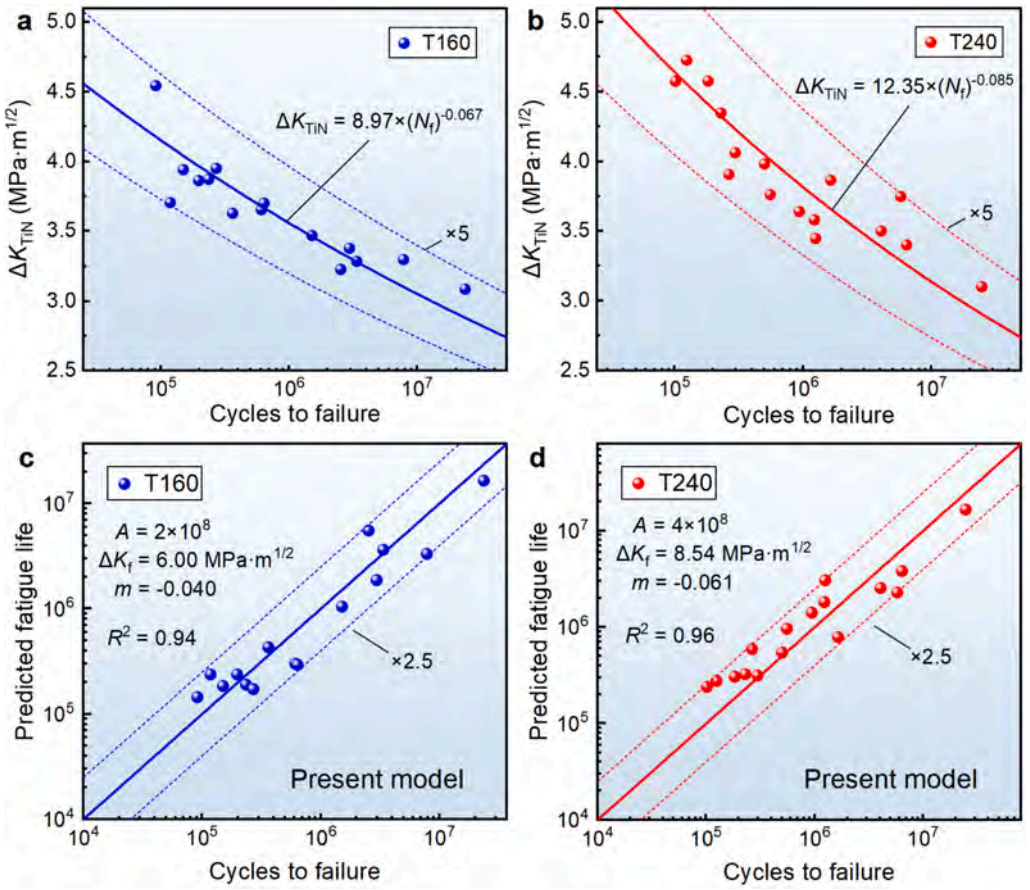

Fig. 11. Comparation between the results obtained by different models. The Murakami model: (a) T160 and (b) T240. Present model: (c) T160 and (d) T240.

on the fatigue life, the relationship between the dimensions of TiN inclusion and the fatigue life predicted by the present model is displayed in Fig. 12a–c. For the effect of size, by assuming $a = b = c$, the relationship between the fatigue life and the size of TiN inclusion can be obtained, as shown in Fig. 12a. It is obvious that the smaller the size is, the higher is the fatigue life. However, it is observed in Fig. 12a that when the inclusion size is greater than a certain value, the fatigue life is unchanged. This is because that the prediction of fatigue life, as described by Eq. (15), is based on the calculation of fatigue life in two distinct stages. Specifically, when the inclusion dimensions are such that $a = b = c$, the fatigue life contribution from the first stage, denoted as N_1, remains constant. However, as the inclusion size exceeds approximately 13 μm, the contribution from the second stage, N_2, decreases rapidly. For instance, at an inclusion size of 13 μm, N_2 is approximately 3000 cycles, whereas at 20 μm, N_2 drops to only 15 cycles. This rapid decay creates an illusion of near constant fatigue life for larger inclusions in Fig. 12a, as the total fatigue life ($N_1 + N_2$) becomes dominated by the constant N_1 term. The underlying limitation arises from Eq. (14) establishing the correlation between ΔK_{TiN} and fatigue life, which assumes constant material parameters ΔK_f and m. Therefore, Eq. (14) should be only valid within the measured inclusion size range.

For the effect of shape, a three-dimensional diagram is displayed in Fig. 12b, utilizing a color map to depict fatigue life. It can be observed that the fatigue lives in two zones are relatively high. To more clearly demonstrate the reasons for the high fatigue lives in these two zones, two examples are provided in Fig. 12c with their fatigue lives decomposed into N_1 and N_2. For type A, $N_1 > N_2$, Eq. (9) dominates the prediction of fatigue life. For type B, however, $N_1 < N_2$, and Eq. (12) is the dominant expression. Accordingly, the schematic illustrations of TiN inclusions in types A and B with different fatigue lives are displayed in Fig. 12d. It can be safely concluded that TiN inclusions in samples with longer fatigue life either have a small area perpendicular to the loading direction or are thin in the direction parallel to the loading.

However, uncertainty still exists in the prediction of fatigue life by the present model, which may stem from several factors impacting fatigue life that the model fails to account for. Firstly, the microstructure of the material matrix, associated with dislocation accumulation behavior, exhibits randomness, yet the model describes this effect using constants. Secondly, the spatial orientation of TiN inclusions, which also influences the efficiency of piling-up of dislocations, has been neglected in the current model. Thirdly, TiN inclusions are not flawless crystal but contain defects that can lead to a reduction in the critical cracking stress. Fourthly, the shape of TiN inclusions is not a perfect rectangle, but rather has some imperfections; however, this point has a relatively small impact. Despite these limitations, our findings and model represent a valuable step forward in understanding and predicting the fatigue behavior of high-strength steels containing TiN inclusions, setting the stage for future refinements and enhancements.

5. Conclusions

In the present study, the fatigue properties of 52100 high-strength steels at two heat treatment states were investigated at room temperature. The TiN inclusions on the fatigue fractures of all samples were examined carefully using SEM and EBSD. Based on the fatigue damage mechanism dominated by the TiN inclusions, a fatigue life prediction model considering the cracking of TiN inclusions was proposed. The following major conclusions can be drawn as below.

1) Extraction experiments conducted on non-fatigued materials confirmed that the actual shape of TiN inclusions is rectangular.

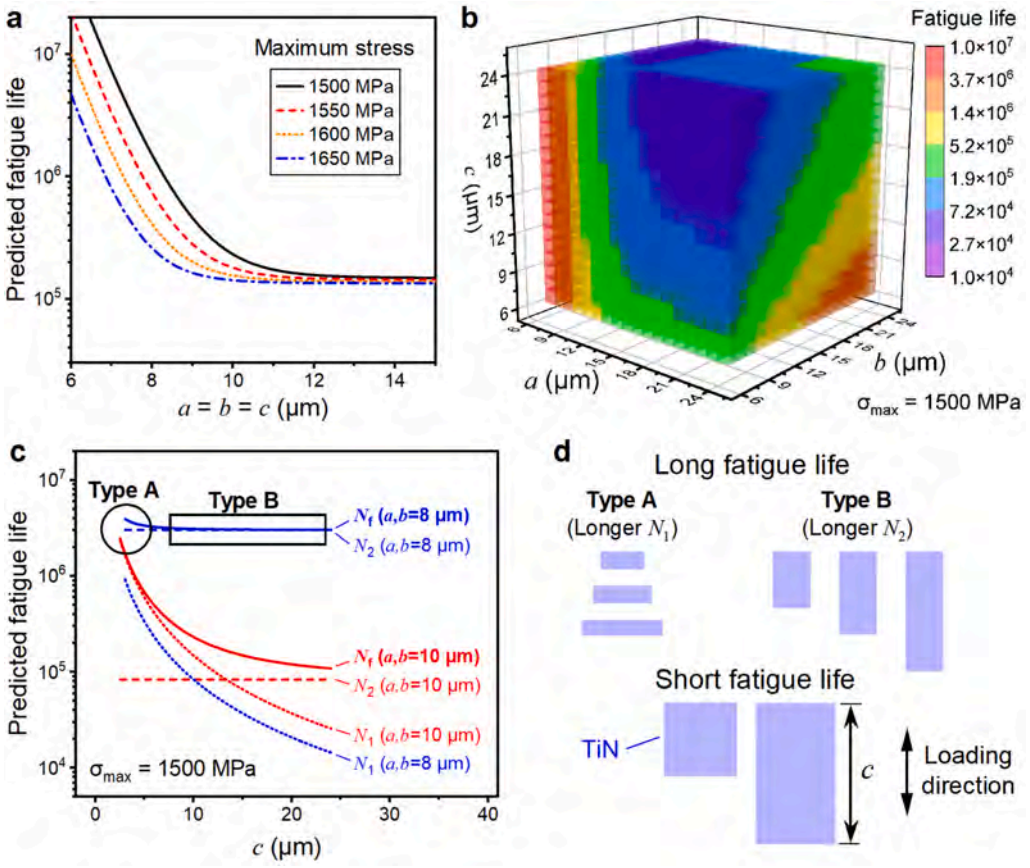

Fig. 12. Effects of the size and shape of TiN inclusion on the fatigue life predicted by the present model: (a) Relationship between the fatigue life and the size of TiN inclusion, assuming $a = b = c$; (b) Relationship between the fatigue life and the parameters a, b and c related to the shape of TiN inclusion; (c) Two examples demonstrate the impact of the shape of TiN inclusion on the stage I and stage II fatigue life; (d) Schematic illustrations of TiN inclusions with different fatigue life.

More than 90 % of the TiN inclusions have a length-to-width ratio below 2.

2) The spatial orientations of TiN inclusions in the samples are randomly distributed, and have no significant effect on their cracking behavior under cyclic stress. All of the examined samples revealed that the fracture plane of TiN inclusions is nearly vertical to the loading axis.
3) A fatigue life prediction model was proposed that takes into account the cracking behavior of TiN inclusions, ultimately reducing the prediction error of fatigue life from within 5 times to 2.5 times.
4) The size and shape of TiN inclusions significantly affect the fatigue lives of the samples. The TiN inclusion in the sample with longer fatigue life either has a small area perpendicular to the loading direction or is thin in the direction parallel to the loading.
5) There are still errors between the predicted fatigue lives by the present model and the experimental fatigue lives due to unaccounted factors such as the randomness of the microstructure, the neglect of the spatial orientations of the TiN inclusions, the crystalline defects in TiN inclusions, and imperfections in the shapes of TiN inclusions.

CRediT authorship contribution statement

Zikuan Xu: Writing – original draft, Methodology, Formal analysis, Data curation, Conceptualization. **Peng Wang:** Investigation. **Yichunxiang Shen:** Investigation. **Peng Zhang:** Investigation. **Bin Wang:** Writing – review & editing. **Ziheng Shao:** Investigation. **Zhefeng Zhang:** Writing – review & editing, Supervision.

Declaration of competing interest

The authors declare that they have no known competing financial interests or personal relationships that could have appeared to influence the work reported in this paper.

Acknowledgments

This work was financially supported by National Key Research and Development Program of China under Grant No. 2022YFB3705200; the National Natural Science Foundation of China (NSFC) under Grant Nos. 52321001, 52130002, 52471150, and 52371123; the IMR Innovation Fund under Grant No. 2024-PY07.

Data availability

Data will be made available on request.

References

[1] Ashby M, Shercliff H, Cebon D. Materials: engineering, science, processing and design. 4th ed. Oxford: Elsevier Ltd; 2019.
[2] Suresh S. Fatigue of materials. 2nd ed. Cambridge, UK: Cambridge University Press; 1998.
[3] Pineau A, Mcdowell DL, Busso EP, Antolovich SD. Failure of metals II: fatigue. Acta Mater 2016;107:484–507.
[4] Kruzic JJ. Predicting fatigue failures. Science 2009;325:156–8.
[5] Bag A, Delbergue D, Bocher P, Lévesque M, Brochu M. Statistical analysis of high cycle fatigue life and inclusion size distribution in shot peened 300M steel. Int J Fatigue 2019;118:126–38.
[6] Wang P, Wang B, Liu Y, Zhang P, Luan YK, Li DZ, et al. Effects of inclusion types on the high-cycle fatigue properties of high-strength steel. Scr Mater 2022;206:114232.

[7] Li SX. Effects of inclusions on very high cycle fatigue properties of high strength steels. Int Mater Rev 2012;57:92–114.
[8] Wang P, Zhang P, Wang B, Zhu YK, Xu ZK, Zhang ZF. Fatigue cracking criterion of high-strength steels induced by inclusions under high-cycle fatigue. J Mater Sci Technol 2023;154:114–28.
[9] Hong YS, Liu XL, Lei ZQ, Sun CQ. The formation mechanism of characteristic region at crack initiation for very-high-cycle fatigue of high-strength steels. Int J Fatigue 2016;89:108–18.
[10] Song QY, Sun CQ. Mechanism of crack initiation and early growth of high strength steels in very high cycle fatigue regime. Mater Sci Eng A 2020;771:138648.
[11] Spriestersbach D, Kerscher E. The role of local plasticity during very high cycle fatigue crack initiation in high-strength steels. Int J Fatigue 2018;111:93–100.
[12] Tanaka K. A theory of fatigue crack initiation at inclusions. Metall Trans A 1982; 13:117–23.
[13] Murakami Y, Kodama S, Konuma S. Quantitative evaluation of effects of non-metallic inclusions on fatigue strength of high strength steels. I: basic fatigue mechanism and evaluation of correlation between the fatigue fracture stress and the size and location of non-metallic inclusions. Int J Fatigue 1989;11:291–8.
[14] Murakami Y, Usuki H. Quantitative evaluation of effects of non-metallic inclusions on fatigue strength of high strength steels. II: fatigue limit evaluation based on statistics for extreme values of inclusion size. Int J Fatigue 1989;11:299–307.
[15] Murakami Y. Metal fatigue: effects of small defects and nonmetallic inclusions. Oxford: Elsevier Science Ltd; 2002.
[16] Zhu ML, Jin L, Xuan FZ. Fatigue life and mechanistic modeling of interior micro-defect induced cracking in high cycle and very high cycle regimes. Acta Mater 2018;157:259–75.
[17] Zhu ML, Zhu G, Xuan FZ. On micro-defect induced cracking in very high cycle fatigue regime. Fatigue Fract Eng Mater Struct 2022;45:3393–402.
[18] Shiozawa K, Lu L, Ishihara S. S-N curve characteristics and subsurface crack initiation behaviour in ultra-long life fatigue of a high carbon-chromium bearing steel. Fatigue Fract Eng Mater Struct 2001;24:781–90.
[19] Murakami Y, Yamashita Y. Prediction of life and scatter of fatigue failure originated at nonmetallic inclusions. Procedia Eng 2014;74:6–11.
[20] Naragani D, Sangid MD, Shade PA, Schuren JC, Sharma H, Park J-S, et al. Investigation of fatigue crack initiation from a non-metallic inclusion via high energy x-ray diffraction microscopy. Acta Mater 2017;137:71–84.
[21] Wang Z, Chen F, Yin Q, Hu B, Luo HW. Complex-inclusion induced fracture mechanism of ultraclean 100Cr6 bearing steel under high cycle fatigue test. Int J Fatigue 2024;184:108310.
[22] Xie ZM, Wang P, Wang B, Zhang P, Bai X, Zhang ZF. Effects of heat treatment on fatigue properties of double vacuum smelting high-carbon chromium-bearing steel. Adv Eng Mater 2022;24:2200151.
[23] Zeng Q, Hui WJ, Zhang YJ, Liu XJ, Yao Z. Very high-cycle fatigue performance of high carbon-chromium bearing steels with different metallurgical qualities. Int J Fatigue 2023;172:107632.
[24] Costa E Silva ALVD. The effects of non-metallic inclusions on properties relevant to the performance of steel in structural and mechanical applications. J Mater Res Technol 2019;8:2408–22.
[25] Xiao W, Bao YP, Gu C, Wang M, Liu Y, Huang YS, et al. Ultrahigh cycle fatigue fracture mechanism of high-quality bearing steel obtained through different deoxidation methods. Int J Min Met Mater 2021;28:804–15.
[26] Sakaguchi R, Shiraiwa T, Chivavibul P, Kasuya T, Enoki M, Yamashita N, et al. Multiscale analysis of MnS inclusion distributions in high strength steel. ISIJ Int 2020;60:1714–23.
[27] Spriestersbach D, Grad P, Kerscher E. Influence of different non-metallic inclusion types on the crack initiation in high-strength steels in the VHCF regime. Int J Fatigue 2014;64:114–20.
[28] Chang R, Morris WL, Buck O. Fatigue crack nucleation at intermetallic particles in alloys—a dislocation pile-up model. Scr Metall 1979;13:191–4.
[29] Fu JW, Nie QQ, Qiu WX, Liu JQ, Wu YC. Morphology, orientation relationships and formation mechanism of TiN in Fe-17Cr steel during solidification. Mater Charact 2017;133:176–84.
[30] Fu JW, Nie QQ, Qiu WX, Sun JJ, Li F, Wu YC. Crystallography and growth mechanism of TiN in Fe-17Cr stainless steel during solidification. J Mater Process Technol 2018;253:43–50.
[31] Xiao YY, Cao L, Wang GC, Wei JF, Sridhar S. Formation and precipitation mechanism of TiN inclusion in Mg-treated GCr15 bearing steel. Metall Mater Trans B 2022;53:916–30.
[32] Prasad K, Sarkar R, Singh V, Ghosal P, Bhattacharjee A, Gokhale H. On the probabilistic assessment of variability in fatigue life in a near α titanium alloy Timetal 834: crystallography of fatigue crack initiating facets. Acta Mater 2021; 218:117214.
[33] Yamashita Y, Murakami Y. Small crack growth model from low to very high cycle fatigue regime for internal fatigue failure of high strength steel. Int J Fatigue 2016; 93:406–14.
[34] Wang ZY, Xing ZG, Wang HD, Shan DB, Huang YF, Xu ZH, et al. The relationship between inclusions characteristic parameters and bending fatigue performance of 20Cr2Ni4A gear steel. Int J Fatigue 2022;155:106594.
[35] Fan YS, Gao GH, Xu X, Liu R, Zhang FM, Gui XL. A fatigue life prediction approach to surface and interior inclusion induced high cycle and very-high cycle fatigue for bainite/martensite multiphase steel. Int J Fatigue 2025;192:108723.
[36] Li C, Zhang YC, Cai L, Hu TY, Wang P, Li XL, et al. A fatigue life prediction approach to interior cracking induced high cycle and very high cycle fatigue for surface-carburized steels. Fatigue Fract Eng Mater Struct 2022;45:865–81.
[37] Liu YB, Yang ZG, Li YD, Chen SM, Li SX, Hui WJ, et al. Dependence of fatigue strength on inclusion size for high-strength steels in very high cycle fatigue regime. Mater Sci Eng A 2009;517:180–4.
[38] Li DZ, Wang P, Chen XQ, Fu PX, Luan YK, Hu XQ, et al. Low-oxygen rare earth steels. Nat Mater 2022;21:1137–43.
[39] Sinha V, Pilchak AL, Jha SK, Porter WJ, John R, Larsen JM. Correlating scatter in fatigue life with fracture mechanisms in forged Ti-6242Si alloy. Metall Mater Trans A 2018;49A:1061–78.
[40] Aigner K, Lengauer W, Rafaja D, Ettmayer P. Lattice parameters and thermal expansion of $Ti(C_xN_{1-x})$, $Zr(C_xN1-x)$, $Hf(C_xN_{1-x})$ and TiN_{1-x} from 298 to 1473 K as investigated by high-temperature X-ray diffraction. J Alloys Compd 1994;215: 121–6.
[41] Lankford J, Kusenberger FN. Initiation of fatigue cracks in 4340 steel. Metall Trans 1973;4:553–9.
[42] Cottrell AH. Dislocations and plastic flow in crystals. New York: Oxford University Press; 1953.